Hole energy levels and intersubband absorption in modulation-doped $Si/Si_{1-x}Ge_x$ multiple quantum wells

T. Fromherz, E. Koppensteiner, M. Helm, and G. Bauer
Institut für Halbleiterphysik, Universität Linz, A-4040 Linz, Austria

J. F. Nützel and G. Abstreiter
Walter Schottky Institut, Technische Universität München, D-85748 Garching, Germany
(Received 20 June 1994)

A theoretical and experimental study of intersubband transitions in modulation-doped *p*-type Si/SiGe quantum wells is presented for SiGe wells with widths between 26 and 65 Å and Ge contents in the range from 19% to 50%. The SiGe multiple quantum wells are pseudomorphically strained with an in-plane lattice constant equal to the lattice constant of the Si substrate. Calculations of the in-plane dispersion of the quantum-well states are performed within the envelope-function approach, with full inclusion of the degeneracy and warping of the three topmost bulk valence bands described by the strain-dependent Luttinger-Kohn Hamiltonian. Many-body effects such as the Hartree potential and the exchange-correlation interaction are taken into account in a self-consistent manner. The transmission spectra are finally calculated with a dielectric simulation for the multilayer stack. Using the structural parameters determined by high-resolution triple-axis x-ray diffraction, the results of the calculation are in excellent agreement with the observed intersubband absorption that occurs between 480 and 1830 cm^{-1} for the different samples. As long as the excited states are confined to the SiGe wells, the full widths of the absorption lines are only 20 meV. This value represents the narrowest absorption line so far observed in *p*-type SiGe quantum wells.

I. INTRODUCTION

Intersubband transitions in semiconductor quantum wells have been studied extensively in the past few years.[1] On the one hand they represent a valuable tool for the spectroscopic study of low-dimensional semiconductor systems, and on the other hand they have high potential concerning technological applications for infrared light emitters and even lasers[2] as well as detectors.[3,4] The material system which has been most extensively studied is the $GaAs/Al_xGa_{1-x}As$ system, but recently the Si/SiGe system has attracted a lot of attention, mainly due to the impressive progress in growth technology. Additionally, the Si/SiGe system has the obvious advantage of being compatible with silicon-integrated technology.

Several different ways of confining carriers can be achieved in the Si/SiGe system, depending on the substrate material and the strain configuration. For example, when grown on Si, most of the band offset occurs in the valence band, so only holes can be effectively confined in the SiGe layers. The confinement of electrons requires an in-plane lattice constant different from Si, which can be achieved by growing a thick, relaxed SiGe buffer layer before the active material. A breakthrough in growing high-quality buffers recently occurred through the concept of the graded buffer, where the Ge content is ramped continuously or stepwise to the desired value.[5–7] In such systems, electrons can be confined either in Si layers or in alloy layers with a Ge content exceeding 80%,[8] depending on the strain. In both cases intersubband absorption has been demonstrated experimentally.[9–12]

In a simple, isotropic, single-valley band structure, intersubband transitions can only be excited with light polarized perpendicular to the layers, (i.e., parallel to the growth direction—this will be our terminology from now on). However, this selection rule can be relaxed in more complicated configurations. It has been shown recently[11–13] that intersubband transitions for light polarized perpendicular to the growth direction are allowed if the quantum-well states are built up from ellipsoidal energy valleys which are tilted with respect to the growth direction. In the Si/SiGe system, this can be realized for *n*-type quantum wells by growing a Si well on a (110)-oriented SiGe buffer[11] or by growing a Ge well on a (100) SiGe buffer.[12] In addition, as shown by the theoretical work of Chang and James[14] and Chun, Pan, and Wang,[15] intersubband transitions for light polarized perpendicular to the growth direction are also allowed between valence-band quantum-well states which are built up from different bulk valence bands [heavy hole (HH), light hole (LH), and spin split-off (SO)]. Experimentally, in *p*-type Si/SiGe quantum wells such transitions have been observed recently.[16,17] Therefore, this issue makes the hole system in SiGe quantum wells attractive for infrared detector application, since normal-incidence absorption is possible under certain conditions. In addition, such structures can be grown pseudomorphically on [001] Si substrates, and thus show the highest structural quality of all quantum-well structures so far realized in the Si/SiGe system. From the technological point of view this type of structure is also preferable, since thick buffers are unwanted for commercial applications.

 ©1994 The American Physical Society

The intersubband absorption of holes in SiGe quantum wells has been reported in a number of publications.[16–18] In the majority of this work, the SiGe quantum wells were heavily p-type doped, resulting in very broad absorption lines. On the other hand, a number of calculations of the valence-band structure of these systems has been published,[15,17,19] but a complete understanding of the absorption has not been achieved to date.

In the present paper we report on intersubband absorption in a larger number of SiGe quantum wells with widely different structural parameters, which were all determined accurately by triple-axis high-resolution x-ray-diffraction and reciprocal space mapping. The samples were modulation doped and exhibit the narrowest absorption lines in p-type SiGe quantum wells so far. For all the samples a full, self-consistent Luttinger-Kohn-type band-structure calculation[20] is performed, including strain, in-plane dispersion, and many-body effects. In addition, the dielectric function is calculated from the band structure and fed into a dielectric simulation to calculate the actual sample transmission. This comparison enables us to obtain an accurate understanding of the origin of the transitions involved in the absorption process.

The paper is organized as follows: In Sec. II we describe the sample parameters together with their determination by x-ray diffraction, as well as the experimental procedure for the infrared measurements. In Sec. III we present the band-structure calculation on the basis of the strain-dependent Luttinger-Kohn $\mathbf{k}\cdot\mathbf{p}$ scheme[20] as well as the calculation of the dielectric function. In Sec. IV some important results of this calculation are discussed on the basis of one specific sample structure. This includes the discussion of the dielectric simulation, which shows the occurrence of the Berreman effect.[21] In Sec. V the experimental results are presented and compared to the calculations, which is followed by conclusions in Sec. VI.

II. SAMPLE STRUCTURE AND EXPERIMENTAL PROCEDURE

The Si/SiGe multiple quantum wells (MQW's) were grown by molecular-beam epitaxy (MBE) in a commercial growth chamber (Riber SIVA 32) at the Walter Schottky Institute on semi-insulating (100) Si wafers. The growth temperature was varied between 400 and 550 °C in the multiple-quantum-well sequence, and the total growth rate between 0.02 and 0.4 Å/s in order to obtain maximum surface flatness and minimal interface mixing. The wafers were not rotated during growth. This results in controlled variations of the Ge content and well and barriers widths of the MQW across one wafer, and allows for a systematic study of the dependence of the transition energy and the line shape of intersubband absorption on these parameters. The samples investigated in this work consist of ten SiGe alloy quantum wells, separated by approximately 180-Å Si barriers, the 60-Å center of which is boron doped. The MQW samples were taken from four different wafers. From each wafer samples with nearly equal well widths, but different Ge content, were taken. The approximate well widths on the respective wafers were 65, 45, 30, and 27 Å. Whereas on the first three wafers the Ge content in the quantum wells varied from 19% to 30%, the fourth wafer contains deeper quantum wells with a Ge content between 42% and 50%. The doping level in the first three wafers was 2.2×10^{18} cm^{-3}, and in the fourth wafer 7.0×10^{17} cm^{-3}. The Hall mobility of the samples is in the range between 200 and 300 cm^2/V s at 4.2 K.

The exact structural parameters (listed in Table I) and the strain status were determined by high-resolution triple-axis x-ray diffraction and reciprocal space mapping. In Fig. 1, the high-resolution triple-axis x-ray-diffraction patterns of two samples are shown. Superlattice satellites up to the sixth order were observed for a MQW with 25% Ge content. Due to the higher x-ray-scattering cross section of Ge as compared to Si, more superlattice satellites (up to the ninth order) could be observed for the MQW with the higher Ge content. Also shown in Fig. 1 are the results of a simulation of the x-ray-diffraction patterns based on the dynamical diffraction theory[22] using the parameter indicated in the plot. Excellent agreement is achieved between measurement and simulation. Furthermore, eight subsidiary maxima between the lowest-order superlattice satellites are clearly resolved. Their mutual distance corresponds to the finite thickness of the system of ten quantum wells. The appearance of these finite thickness fringes in the diffraction pattern indicates the high structural quality of the samples investigated in this work.

Information concerning the strain status is contained in the reciprocal space maps as presented in Fig. 2. It shows the reciprocal space maps for the (004) and (224) Bragg reflections for a multiple quantum well with a width of 27 Å and a Ge content of 50%. Plotted are the contours of constant scattered x-ray intensity. Apart from the Si substrate peak, the main superlattice peak (SL0) and the first-order peak (SL1) are shown. In the (004) map, the finite thickness fringes (labeled 1–8) are observed between the SL0 and SL1 reflexes. Their distance is equal to $1/nL$, where L denotes the length of one period and n is the number of periods within one sample

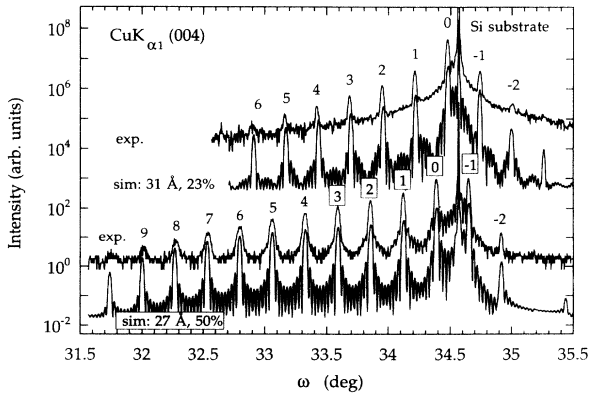

FIG. 1. Measured and simulated high-resolution triple-axis x-ray-diffraction patterns of two Si/SiGe MQW's. The numbers indicate the order of the superlattice satellites. In the simulation, the width (Ge content) of the quantum wells was assumed to be 31 Å (23%) and 27 Å (50%), respectively.

TABLE I. Structural parameters of the MQW's investigated in this work as determined by high-resolution triple-axis x-ray diffraction.

Well width (Å)	Ge content (%)	Barrier width (Å)
65	23	198
64	26	184
60	30	163
49	21	196
47	25	181
44	31	164
36	19	180
31	23	177
26	27	160
27	42	206
27	50	175

($n=10$ for the present samples). In the (004) reciprocal space map, the intensity contours inclined by approximately 45° relative to the [001] direction are an experimental artifact due to the high intensity of the (004) Bragg reflex of the Si substrate. In the (224) reciprocal space map, the extrema of the SL0 and SL1 peaks are aligned along a line parallel to the [100] direction through the maximum intensity of the Si substrate (224) reciprocal-lattice point. In addition, perpendicular to the [001] direction, the full width at half maximum (FWHM) of the SL peaks is equal to the FWHM of the Si substrate peak, and therefore is determined only by the angular resolution of the x-ray diffractometer (12 in.). Thus *all* the layers building up the Si/SiGe multiple-quantum-well system have the same in-plane lattice constant as the substrate.[23] Therefore, the reciprocal space maps show that even for the samples with the highest Ge concentration (50%) the SiGe quantum wells are pseudomorphically strained.

Infrared-absorption measurements were performed in a Bruker IFS 113 Fourier transform spectrometer at a temperature of 12 K. The samples were prepared in multipass waveguide geometry.[9] The radiation is coupled into the sample at one facet which is wedged at an angle of 38°, and then undergoes approximately seven (depending on the ratio of the thickness to the length of the sample) total internal reflections at a reflection angle of 52°. On top of the multiple-quantum-well structure, a layer of gold (300 nm) was deposited in order to enhance the electric field of infrared radiation polarized parallel to the growth direction.[24] The transmission spectra were measured both in *p* polarization (electric field parallel to the growth direction) and *s* polarization (electric field perpendicular to the growth direction). The ratio of the transmitted intensity of *p*- and *s*-polarized radiations was normalized to the respective ratio for the reference Si substrate prepared in the same manner as the multiple-quantum-well samples. By this normalization, any polarization-dependent signal that does not originate from the MQW's, but from the Si substrate or the optical components of the spectrometer, can be removed from the spectra.

III. THEORY

For calculating the energy levels in a *p*-type SiGe quantum well a suitable description of the valence bands in bulk Si and Ge is needed. According to the **k·p** theory, the highest valence bands, including heavy-hole (HH),

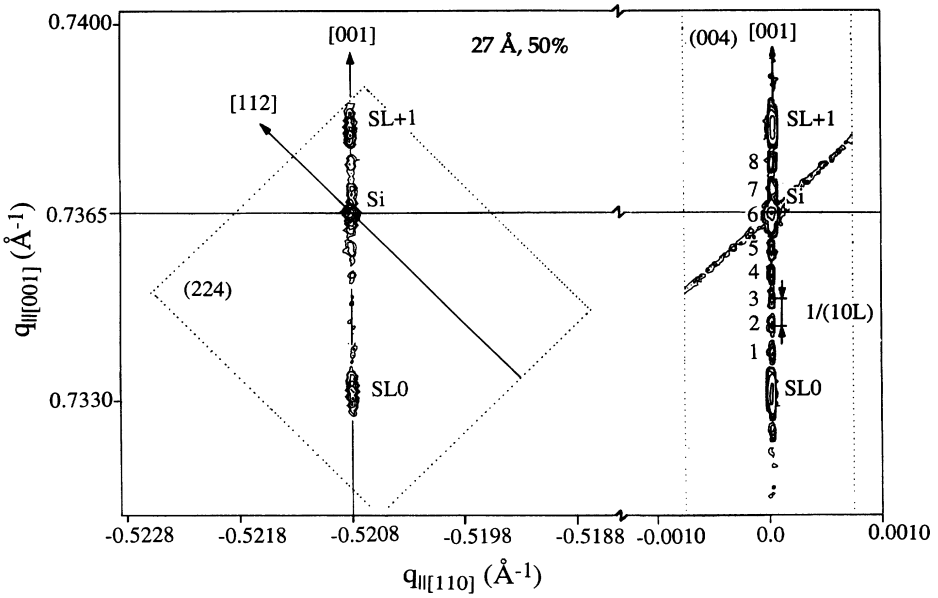

FIG. 2. Reciprocal space maps for the (004) and (224) Bragg reflections of a Si/SiGe MQW with a width of 27 Å and a Ge content of 50%. Plotted are the contours of constant scattered x-ray intensity. The (224) map shows that the MQW structure is pseudomorphically strained since the extrema of the SL0 and SL1 peaks are aligned along a line parallel to the [001] direction through the maximum intensity of the Si substrate (224) reciprocal-lattice point. In addition, for the [110] direction (in-plane) the FWHM of the Si substrate peak and the superlattice satellites are equal and, therefore, no misfit dislocations are present at the interfaces. In the (004) map, the eight subsidiary maxima between the SL0 and SL+1 correspond to the total number (ten) of quantum wells. Their distance is equal to $1/10L$, where L denotes the period of the MQW structure.

light-hole (LH), and spin-split-off (SO) bands near the zone center, are well described by diagonalizing a 6×6 Luttinger-Kohn Hamiltonian $H^0(k)$.[20,25,26] By choosing the cell periodic functions

$$|u^{\mathbf{k}}_{j,m}\rangle = |u^0_{j,m}\rangle - \frac{\hbar}{m_0}\sum_s \frac{\langle u_s|\mathbf{k}\cdot\boldsymbol{\pi}|u^0_{j,m}\rangle}{E_s}|u_s\rangle \quad (1)$$

as a basis, $H^0(k)$ is decoupled from the remote bands $|u_s\rangle$ to the second order, and has the following form:[20,25]

$$H^0_{\nu'\nu}(\mathbf{k}) = \sum_{\alpha\beta} k_\alpha D^{\alpha\beta}_{\nu'\nu} k_\beta + \delta_{\nu'\nu}E^0_\nu ,$$

$$\nu=(j,m),\quad \alpha,\beta=(x,y,z) . \quad (2)$$

Here E^0_ν is the energy of the valence band ν at the Γ point, and $D^{\alpha\beta}_{\nu'\nu}$ are the inverse mass matrices and are defined as[20,25]

$$D^{\alpha\beta}_{\nu'\nu} = \frac{\hbar^2}{2m_0}\left[\delta_{\nu'\nu}\delta_{\alpha\beta} - \frac{1}{m_0}\sum_s \frac{\pi^\alpha_{\nu's}\pi^\beta_{s\nu} + \pi^\beta_{\nu's}\pi^\alpha_{s\nu}}{E_s}\right] . \quad (3)$$

Here $\boldsymbol{\pi}$ is the momentum operator including the spin-orbit interaction defined by[20,25]

$$\boldsymbol{\pi} = \frac{\hbar}{i}\nabla + \frac{\hbar}{4mc^2}(\boldsymbol{\sigma}\times\nabla V) . \quad (4)$$

Because of the symmetry of the diamond lattice, $D^{\alpha\beta}_{\nu'\nu}$ are determined by only three different parameters γ_1, γ_2, and γ_3 (Luttinger parameters). The explicit form of $H^0_{\nu'\nu}(\mathbf{k})$ is[20,26]

$$H^0_{\nu'\nu}(\mathbf{k}) = \begin{pmatrix} H_{\rm HH} & S & -T & 0 & \frac{i}{\sqrt{2}}S & i\sqrt{2}T \\ S^* & H_{\rm LH} & 0 & -T & -iV & i\sqrt{\frac{3}{2}}S \\ -T^* & 0 & H_{\rm LH} & -S & i\sqrt{\frac{3}{2}}S^* & -iV \\ 0 & -T^* & -S^* & H_{\rm HH} & i\sqrt{2}T^* & \frac{-i}{\sqrt{2}}S^* \\ \frac{-i}{\sqrt{2}}S^* & iV & i\sqrt{\frac{3}{2}}S & -i\sqrt{2}T & H_{\rm SO} & 0 \\ -i\sqrt{2}T^* & -i\sqrt{\frac{3}{2}}S^* & iV & \frac{i}{\sqrt{2}}S & 0 & H_{\rm SO} \end{pmatrix} , \quad (5a)$$

where

$$H_{\rm HH} = -\frac{\hbar^2}{2m_0}[k_z(\gamma_1-2\gamma_2)k_z + (\gamma_1+\gamma_2)(k_x^2+k_y^2)] + \frac{\Delta_0}{3} , \quad (5b)$$

$$H_{\rm LH} = -\frac{\hbar^2}{2m_0}[k_z(\gamma_1+2\gamma_2)k_z + (\gamma_1-\gamma_2)(k_x^2+k_y^2)] + \frac{\Delta_0}{3} , \quad (5c)$$

$$H_{\rm SO} = -\frac{\hbar^2}{2m_0}[k_z\gamma_1 k_z + \gamma_1(k_x^2+k_y^2)] - \frac{2\Delta_0}{3} , \quad (5d)$$

$$S = \frac{\sqrt{3}\hbar^2}{2m_0}(k_x - ik_y)(k_z\gamma_3 + \gamma_3 k_z) , \quad (5e)$$

$$T = -\frac{\sqrt{3}\hbar^2}{2m_0}[\gamma_2(k_x^2-k_y^2) - 2i\gamma_3 k_x k_y] , \quad (5f)$$

$$V = -\frac{\sqrt{2}\hbar^2}{2m_0}[\gamma_2(k_x^2+k_y^2) - 2k_z\gamma_2 k_z] , \quad (5g)$$

and Δ_0 is the spin-orbit splitting of the valence bands at the Γ point.

Biaxial strain in the (x,y) plane lifts the degeneracy of the heavy- and light-hole bands at the Γ point and mixes light-hole and spin-split-off bands. In $H^0_{\nu'\nu}(\mathbf{k})$ the strain enters by replacing $H_{\rm HH}$ by $H_{\rm HH}+\varepsilon$, $H_{\rm LH}$ by $H_{\rm LH}-\varepsilon$, and $V+\varepsilon\sqrt{2}$,[26,27] where ε is determined by the biaxial in-plane strain ε_{xx}, the elastic constants c_{11} and c_{12}, and the deformation potential parameter b as follows:[26,27]

$$\varepsilon = b\left[\frac{2c_{12}}{c_{11}} + 1\right]\varepsilon_{xx} ,$$

$$\varepsilon_{xx} = \frac{a_{\rm strain} - a_0}{a_0} . \quad (6)$$

Here a_0 is the lattice of the unstrained crystal, and $a_{\rm strain}$ is the in-plane lattice constant of the biaxially strained crystal.

For pure Si and Ge the valence-band parameters (γ_i), the spin-orbit splitting Δ_0, and the lattice parameters (a_0, c_{ij}) are taken from literature.[28] For SiGe the lattice parameters and the spin-orbit splitting are obtained by linear interpolation between the values for pure Si and Ge. According to Ref. 8, the valence-band parameters for SiGe are nonlinearly interpolated between the experimentally determined values of Si and Ge reported in the literature. The results of this interpolation are shown in Fig. 3.

If the growth direction of the superlattice is chosen to be the z direction, k_z is no longer a good quantum num-

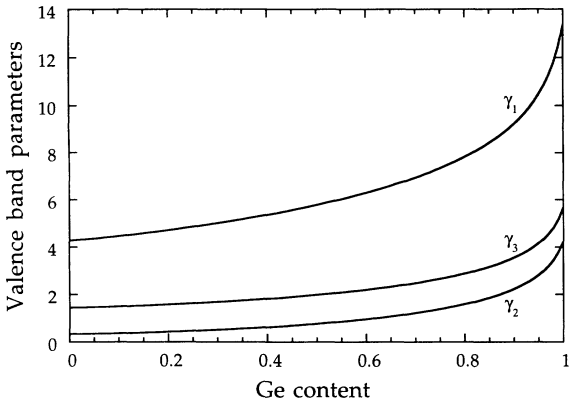

FIG. 3. Dependence of the valence-band parameters of a SiGe alloy on the Ge content as used in this work. The interpolation between the valence-band parameters of Si and Ge was performed according to Ref. 8.

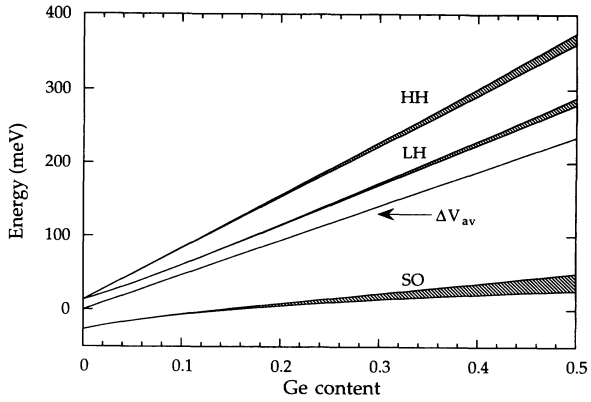

FIG. 4. Band offset of the HH, LH, and SO valence bands at a Si/SiGe interface for pseudomorphically strained SiGe as used in this work. The value of ΔV_{av} was calculated by Colombo, Resta, and Baroni with *ab initio* methods (Ref. 31). The hatched areas indicate the uncertainty of the band offsets due to the uncertainty in the deformation potential of Ge.

ber. Therefore, under the usual assumption in the envelope-function approach that the basis $|u_{j,m}\rangle$ is the same in both materials of the superlattice, k_z is replaced by the operator $-i(\partial/\partial z)$ in the expression for $H^0_{\nu'\nu}(\mathbf{k})$.[29,30] In addition, the band parameters, the spin-orbit splitting, and ε are position dependent. Following Refs. 29 and 30, in this case the superlattice Hamiltonian has the form

$$H_{\nu'\nu}\left[k_x,k_y,-i\frac{\partial}{\partial z};z\right] = H^0_{\nu'\nu}\left[k_x,k_y,-i\frac{\partial}{\partial z};z\right]+\delta_{\nu'\nu}V_{\mathrm{SL}}(z)\,, \quad (7)$$

where the definition of $H^0_{\nu'\nu}(\mathbf{k})$ ensures that $H_{\nu'\nu}$ is Hermitian. The superlattice potential V_{SL} is approximated by the sum of three contributions; the barrier potential ΔV_{av}, the Hartree potential V_H, and the exchange correlation potential V_{xc}. In the following we discuss each of these contributions.

The definition of the strain-dependent Luttinger-Kohn Hamiltonian $H^0_{\nu'\nu}(\mathbf{k})$ [Eqs. (5) and (6)] ensures that the average energy of the three valence bands at the Γ point is constant (zero) for all values of the strain (ε_{xx}). Strain and spin-orbit interaction (Δ_0) cause a splitting of the three valence bands around this constant energy value. Thus, at a heterointerface between Si and SiGe, the alignment of the HH, LH, and SO bands at the Γ point can be calculated once the offset of the average energy of the three valence bands (ΔV_{av}) and the strain in the Si and SiGe layers is known. The value of ΔV_{av} has been calculated with *ab initio* methods for a strained Si-Ge interface by Colombo, Resta, and Baroni.[31] For the case of pseudomorphically grown Ge on unstrained Si, they obtained $\Delta V_{av}=470$ meV. In agreement with Ref. 32 we assume that ΔV_{av} varies linearly with the Ge content of the strained SiGe layer. Figure 4 shows the alignment of the HH, LH, and SO bands calculated by diagonalizing $H^0_{\nu'\nu}(\mathbf{k})$ at $\mathbf{k}=0$ for unstrained Si and pseudomorphically strained SiGe. The hatched regions in Fig. 4 indicate the uncertainty in the band alignments due to the different values of the deformation potential (b_{Ge}) of Ge reported in literature (e.g., Refs. 8, 27, and 28). The borders of the hatched regions correspond to $b_{\mathrm{Ge}}=-2$ and -2.8 eV. In the following calculations we use a value of $b_{\mathrm{Ge}}=-2.4$ eV.

The Hartree potential V_H arises from the charge distribution within the superlattice and is the solution of Poisson's equation

$$\nabla^2 V_H=\frac{e^2}{\varepsilon\varepsilon_0}\left[\sum_{\text{occupied}}\chi_i^*(\mathbf{r})\chi_i(\mathbf{r})-N_A^-(\mathbf{r})\right], \quad (8)$$

where $\varepsilon\varepsilon_0$ denotes the dielectric constant, e is the elementary charge, and N_A^- is the concentration of occupied acceptors. V_H has to be calculated in a self-consistent loop, as it is determined by the envelope functions χ_i. For SiGe quantum wells pseudomorphically grown on a Si substrate, only the heavy-hole subband is occupied at low temperature due to the strain-induced splitting of heavy- and light-hole subbands. If we assume that the squared modulus of the envelope functions χ_i for the heavy-hole subband is independent of the in-plane wave vector (k_x,k_y), V_H can be calculated from the envelope function belonging to a particular in-plane wave vector. Since at the Γ point ($k_x=k_y=0$) the heavy-hole band is decoupled from the other valence bands [see Eq. (5)], V_H is determined by

$$\nabla^2 V_H=\frac{e^2}{\varepsilon\varepsilon_0}[p_s\chi^*_{\mathrm{HH},0}(z)\chi_{\mathrm{HH},0}(z)-N_A^-(z)]\,, \quad (9)$$

where $\chi_{\mathrm{HH},0}$ is an eigenfunction of $H_{11}[0,0,-i(\partial/\partial z);z]$, and p_s is the sheet concentration of free holes per period. Therefore, the self-consistent Hartree potential can be calculated in a one-band model. The validity of the above assumption can be checked *a posteriori*. For the samples investigated in this work, this assumption is an

excellent approximation.

The effects of exchange correlation can be included through a one-particle exchange-correlation potential energy $V_{xc}[p(\mathbf{r})]$, where $p(\mathbf{r})$ is the hole density of the well.[33] Using the same arguments as in the previous paragraph, $p(\mathbf{r})$ can be expressed by $p(z)=p_s\chi^*_{HH,0}\chi_{HH,0}$. We approximate the exchange-correlation potential energy by the interpolation formula given by Hedin and Lundqvist:[34]

$$V_{xc}=-2\left[\frac{9}{4\pi^2}\right]^{1/3}\frac{e^2}{8\pi\varepsilon\varepsilon_0 a_0}\times\frac{1}{r_s}\left[1+\frac{B}{A}r_s\ln\left[1+\frac{A}{r_s}\right]\right], \tag{10}$$

where $A=21$, $B=0.7734$, $a_0=(\varepsilon/m^*)a_B$, $r_s=[4\pi a_0^3 p(z)/3]^{-1/3}$, and a_B is the Bohr radius. Since in the ground state the holes are confined to the SiGe layers, for ε and m^* we have chosen the values of the dielectric constant of SiGe and the heavy-hole mass of SiGe along the (100) direction, respectively. Again, as V_{xc} is determined by the envelope function $\chi_{HH,0}$, it is to be calculated in a self-consistent way.

Having calculated the self-consistent contributions to V_{SL} in a one-band model, the full 6×6 superlattice Hamiltonian [Eq. (7)] can be diagonalized. The envelope functions χ_ν are the solutions of the six coupled differential equations:

$$\sum_\nu\left[H_{\nu'\nu}\left[k_x,k_y,-i\frac{\partial}{\partial z};z\right]-\delta_{\nu'\nu}E\right]\chi_\nu=0\ . \tag{11}$$

We have solved this system by expanding the envelope functions χ_ν in Fourier series. For periodic boundary conditions we make the following ansatz according to the Bloch theorem:

$$\chi_\nu=e^{iqz}\sum_{k_z}c_\nu^{k_z}(k_x,k_y,q)e^{ik_z z}\ , \tag{12}$$

where

$$k_z=\frac{2\pi}{L}n\ ,$$

$$n=0,\pm1,\pm2,\ldots,$$

$$q\in\left]-\frac{\pi}{L},\frac{\pi}{L}\right]\ .$$

Here L denotes the period of the superlattice in the growth direction. Inserting the ansatz into Eq. (11), multiplying Eq. (11) with $e^{-i(q+k_z')z}$ from the left side, and integrating over L transforms Eq. (11) into a $6m\times6m$ matrix eigenvalue problem for the coefficients $c_\nu^{k_z}$:

$$\sum_{\nu,k_z}[H_{\nu'\nu}^{k_z'k_z}(k_x,k_y,q)-\delta_{\nu'\nu}\delta_{k_z'k_z}E_n]c_{\nu;n}^{k_z}=0\ , \tag{13}$$

where

$$H_{\nu'\nu}^{k_z'k_z}(k_x,k_y,q)=\int_0^L\frac{dz}{L}e^{-i(q+k_z')z}H_{\nu'\nu}\left[k_x,k_y,-i\frac{\partial}{\partial z};z\right]e^{i(q+k_z)z}\ . \tag{14}$$

Here m denotes the number of plane waves included in the expansion of the envelope function. In our calculation, typically 17 plane waves were used for the diagonalization of $H_{\nu'\nu}^{k_z'k_z}$. Including more than 17 plane waves results in a change of the first 20 eigenenergies of less than 1 meV. Due to the confining potential and the strain, the valence bands ν become mixed for the finite in-plane wave vector; i.e., for an eigenstate n the Fourier coefficients $c_{\nu;n}^{k_z}$ are finite in different subspaces ν. For confining potentials with inversion symmetry, the eigenvalues E_n are doubly degenerate (Kramers degeneracy).

The optical properties of the superlattice are completely determined by the dielectric tensor $\varepsilon_{\alpha\beta}$, the imaginary part of which is related to the real part of the conductivity tensor $\sigma_{\alpha\beta}$ by $\mathrm{Im}(\varepsilon_{\alpha\beta})=\mathrm{Re}(\sigma_{\alpha\beta})/\varepsilon_0\omega$. Once $\mathrm{Im}(\varepsilon_{\alpha\beta})$ is known, the real part can be calculated by a Kramers-Kronig transformation. From symmetry, for a Si/SiGe superlattice with growth direction along the z axis, the off-diagonal elements of ε vanish and $\varepsilon_{xx}=\varepsilon_{yy}$. At $T=0$ K the intersubband contribution to $\mathrm{Re}(\sigma_{\alpha\alpha})$ can be calculated[25] as

$$\mathrm{Re}(\sigma_{\alpha\alpha}(\omega))=-\frac{\pi}{\hbar\omega V}\sum_{m,n}|j_{m,n}^\alpha|^2\delta(\omega-\omega_{mn})\ . \tag{15}$$

The summation extends over all occupied superlattice hole states m and all empty superlattice hole states n, ω is the frequency of the incident light, and $\hbar\omega_{mn}=E_m-E_n$. In the numerical calculations, the δ function in Eq. (15) was replaced by a Lorentz curve, the broadening parameter of which was used as a fitting parameter. Since spin-orbit interaction is included, the current operator in Eq. (15) is $\mathbf{j}=(e/m_0)\boldsymbol{\pi}$. The matrix elements of $\mathbf{j}$ between the superlattice states

$$\varphi_n=e^{i(k_x x+k_y y)}\sum_\nu\chi_\nu u_\nu=e^{i\mathbf{K}\cdot\mathbf{r}}\sum_{\nu,k_z}c_{\nu;n}^{k_z}(\mathbf{K})e^{ik_z z}u_\nu^{\mathbf{K},k_z}(\mathbf{r})\ , \tag{16}$$

where

$$\mathbf{K}=(k_x,k_y,q)\ ,$$

are given by

$$j_{m,n}^\alpha=\frac{2e}{\hbar}\sum_{\nu'\nu}\sum_{k_z}c_{\nu';m}^{k_z*}c_{\nu;n}^{k_z}\sum_\beta D_{\nu'\nu}^{\alpha\beta}(K_\beta+\delta_{\beta z}k_z)\ . \tag{17}$$

Since the inverse mass matrices $D_{\nu'\nu}^{\alpha\beta}$ contain the bulk selection rules, the transitions allowed in the bulk are also allowed in the superlattice. In the following, we will discuss these selection rules in more detail.

For the samples investigated in this work only the two

topmost spin-degenerate valence subbands (i.e., the lowest hole energy levels) originating from the heavy-hole bands are occupied. It is shown below that the envelope functions for states of these subbands are strongly confined to the SiGe layers, so that for calculating the dielectric tensor the $D^{\alpha\beta}_{\nu'\nu}$ of SiGe were used. In addition we will show in Sec. IV that due to the large strain-induced splitting of the heavy- and light-hole bands, the mixing of the two topmost subbands with the other subbands is very weak. Therefore, in the following discussion of the selection rules we assume that these two subbands are purely heavy-hole-like (i.e., only $c^{k_z}_{1;n}\neq 0$ and $c^{k_z}_{4;n}\neq 0$) for in-plane wave vectors as large as the Fermi wave vector.

The contribution of transitions within the heavy-hole subspace to the total current density [Eq. (17)] is described by the $\nu=\nu'=1,4$ terms in Eq. (17). The corresponding matrices that contain the selection rules (D_{11},D_{44}) are equal to the matrix $H_{\rm HH}$ [see Eq. (5a)], which is defined according to Eq. (5b) as

$$H^{\alpha\beta}_{\rm HH}=-\frac{\hbar^2}{2m_0}\begin{pmatrix}\gamma_1+\gamma_2 & 0 & 0\\ 0 & \gamma_1+\gamma_2 & 0\\ 0 & 0 & \gamma_1-2\gamma_2\end{pmatrix}. \quad (18)$$

For light polarized perpendicular to the growth direction [$\alpha=x,y$ in Eq. (17)], the summation over $\nu=\nu'$ and k_z vanishes in Eq. (17), since different superlattice states are orthogonal, i.e., $\sum_{\nu,k_z} c^{k_z *}_{\nu;m} c^{k_z}_{\nu;n}=0$ for $m\neq n$. For light polarized parallel to the growth direction [$\alpha=z$ in Eq. (17)], the $\nu=\nu'$ and k_z summation in Eq. (17) is finite for superlattice states m,n with Fourier coefficients of opposite parity. The strength of the transitions is determined by the dipole integral $\sum_{\nu,k_z} c^{k_z *}_{\nu;m} k_z c^{k_z}_{\nu;n}$. In conclusion, the matrix $H_{\rm HH}$ allows transitions only for light polarized in the z direction and only between states with finite dipole integral. These selection rules are identical to the well-known selection rules obtained from an envelope-function model, where only one band is included, as is the case for the calculation of superlattice states in the conduction bands.

In addition, transitions between *different subspaces* are allowed. Assuming again that the ground state is purely heavy-hole-like, the contribution of these transitions to the total current density is described by the $\nu'=1,4$ (ground state) and $\nu=2,3,5,6$ (final state) terms in Eq. (17). The D matrices corresponding to any combination of these values of the indices ν and ν' are proportional to either of the matrices T, T^*, S, or S^* [see Eq. (5a)]. According to Eqs. (5e) and (5f) the matrices T and S are defined as

$$T^{\alpha\beta}=-\frac{\sqrt{3}\hbar^2}{2m_0}\begin{pmatrix}\gamma_2 & -i\gamma_3 & 0\\ -i\gamma_3 & -\gamma_2 & 0\\ 0 & 0 & 0\end{pmatrix} \quad (19)$$

and

$$S^{\alpha\beta}=\frac{\sqrt{3}\hbar^2}{2m_0}\begin{pmatrix}0 & 0 & \gamma_3\\ 0 & 0 & -i\gamma_3\\ \gamma_3 & -i\gamma_3 & 0\end{pmatrix}. \quad (20)$$

Since in T all z components vanish, this matrix contributes to the summation in Eq. (17) only for $\alpha,\beta\neq z$, i.e., for light polarized perpendicular to the growth direction, and only for superlattice states with a finite in-plane wave vector. According to Eq. (17), the strength of these transitions is determined by the overlap integral of the Fourier coefficients in the subspaces ν' and ν. Therefore, since the Fourier coefficients of the initial states have even parity with respect to k_z, the Fourier coefficients in the LH or SO subspace of a possible final state must also have a symmetric part.

The matrix S [Eq. (20)] has nonvanishing z components and, therefore, allows transitions for both light polarized perpendicular and parallel to the growth direction. For the parallel polarization ($\alpha=z$), S has nonvanishing components only for $\beta=x,y$ and, therefore, only transitions between superlattice states with finite in-plane wave vector are allowed. Again the strength of these transitions is determined by the overlap integral of the Fourier coefficients in the initial and the final subspace [see Eq. (17)]. For light polarized perpendicular to the growth direction ($\alpha=x,y$), only the $\beta=z$ components of S are nonvanishing and, therefore, transitions for zero in-plane wave vectors are allowed as a direct consequence of the superlattice potential, which couples bulk wave functions with different k_z. In this case, in Eq. (17) the transition strength is determined by the dipole integral. Consequently, the Fourier coefficients within the light-hole or split-off subspaces of a possible excited state must have an antisymmetric part.

To summarize the selection rules, for vanishing in-plane wave vector transitions are only allowed between states of opposite parity. Within the HH subspace, these transitions are only allowed for light polarized parallel to the growth direction, whereas if the final state is outside the HH subspace these transitions are allowed only for light polarized perpendicular to the growth direction. At finite in-plane wave vectors, transitions between states of the same parity also become allowed. For these transitions the final states have to be outside the HH subspace, but they are allowed for both polarizations.

IV. RESULTS OF THE THEORY

In a recent publication, Chun, Pan, and Wang[15] performed similar envelope-function calculations for p-type Si/SiGe quantum wells. However, in their work they concentrated on quantum wells with a sheet carrier density which is approximately ten times higher than the density of the samples investigated in this work. Consequently, the effects of the anisotropy and the nonparabolicity of the energy bands as well as the influences of the many-body interactions, especially the depolarization shift, are much more pronounced in their calculations. Therefore, although some of the results of Chun, Pan, and Wang[15] especially the selection rules and their depen-

dence on the in-plane wave vector, are similar to the results of this work, their calculations are not directly applicable to the samples investigated in this work.

In order to eludicate the results of the theory in the following we will discuss in detail our calculations for the sample with 47-Å well width and 25% Ge content. For this sample, in Fig. 5 the squared moduli of the envelope functions of the first eight energy levels at $k_x = k_y = q = 0$ are shown together with the self-consistent confining potentials for the HH, LH, and SO valence bands. Figure 6(a) shows the in-plane dispersion of the first 13 energy levels along [110]. Each of the levels is twofold spin degenerate. The Fermi energy is approximately 10 meV below the energy of the ground state at $k_x = k_y = 0$. In Fig. 6(b) the squared moduli of the Fourier coefficients in the respective subspaces of the first eight energy bands for an in-plane wave vector along [110] as large as the Fermi wave vector ($k_F \approx 0.03$ Å^{-1}) are shown. According to this plot we labeled the energy levels in Fig. 5 corresponding to the distribution of the Fourier coefficients among the subspaces.

As mentioned in Sec. III, Fig. 6(b) shows that due to the large strain-induced splitting of the heavy-hole and light-hole bands, the topmost energy band in Fig. 6(a) is nearly completely heavy-hole-like for all occupied states. In Fig. 7 the absorption spectra for light polarized both parallel and perpendicular to the growth direction are shown. The broken lines show the spectra calculated for the actual doping level of 1.2×10^{12} cm^{-2}. In order to determine the dependence of the absorption spectra on the in-plane wave vector, we also calculated the absorption spectra for a doping level as low as 3×10^{10} cm^{-2}. The result of this calculation is shown by the full line in Fig. 7. The transition between the bands labeled 1 and 3 in Fig. 6 has the highest oscillator strength. This transition corresponds to the HH1-HH2 transition and, therefore, is only allowed for light polarized parallel to the growth direction. For light polarized perpendicular to the growth direction, the most prominent peak in the calculated absorption spectrum is due to the transitions between the energy bands labeled 1 and 2 in Fig. 6. The final states of these transitions are predominantly a mixture between the ground states in the LH and SO subspace and therefore have the same parity as the initial states (see Fig. 5). Consequently these transitions are only allowed for the nonvanishing in-plane wave vector. The states of the energy bands labeled 4 and 5 in Fig. 6 are barrier bound (see Fig. 5), and therefore do not contribute to the absorption spectrum since they have vanishing overlap with the occupied ground states in real space. The band labeled 6 in Fig. 6 is again mainly a mixture between LH and SO subspaces, but for this band the Fourier coefficients have opposite parity from the ground

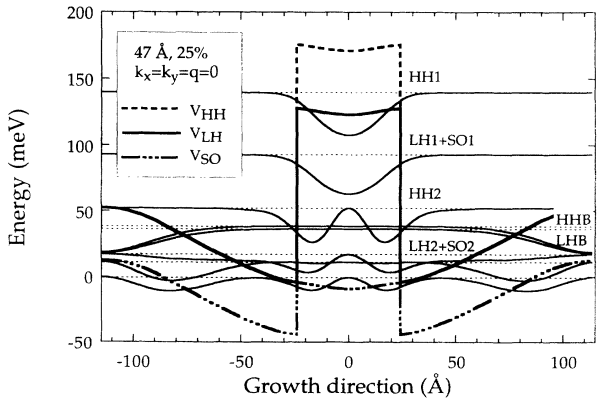

FIG. 5. Results of the self-consistent calculation of the valence-band states in a 47-Å quantum well with 25% Ge content. Shown are the squared moduli of the envelope functions (thin solid lines) of the first eight energy levels (thin broken lines) at $k_x = k_y = q = 0$, and the self-consistent confining potentials for the HH, LH, and SO bands (bold lines). The energy levels are labeled according to the bulk valence bands that build up the quantum-well state predominantly.

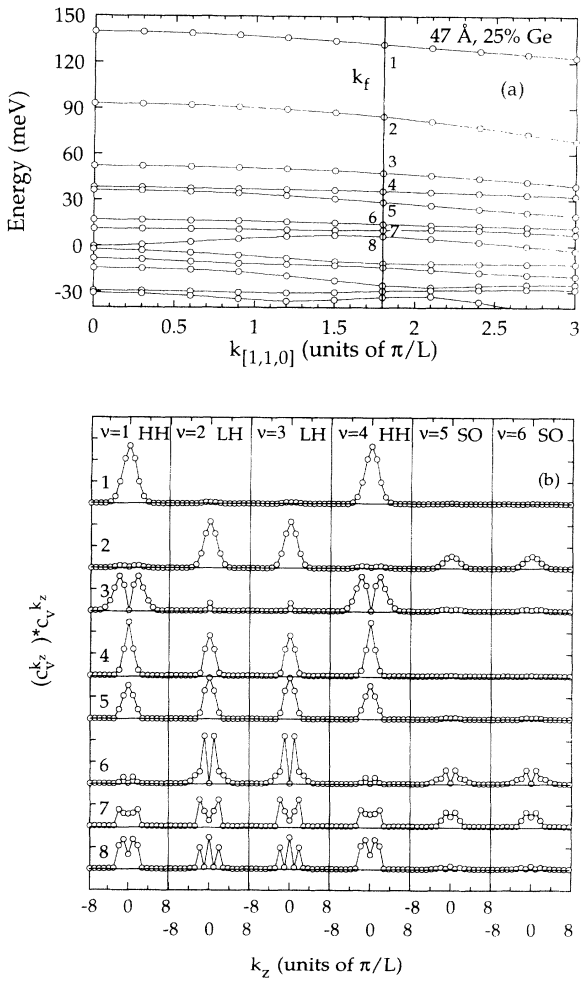

FIG. 6. Results of the self-consistent calculation of the valence-band states in a 47-Å quantum well with 25% Ge content. The dispersion of the first 13 energy levels for an in-plane wave vector parallel to the [110] direction is shown in (a). Also indicated in (a) is the Fermi wave vector k_f corresponding to the carrier sheet concentration of 1.2×10^{12} cm^{-2} ($k_f \approx 0.03$ Å^{-1}). In (b) the squared moduli of the Fourier coefficients in the six subspaces included in our calculation are shown for the first eight quantum-well states at the Fermi wave vector in [110] direction [labeled 1–8 in (a)].

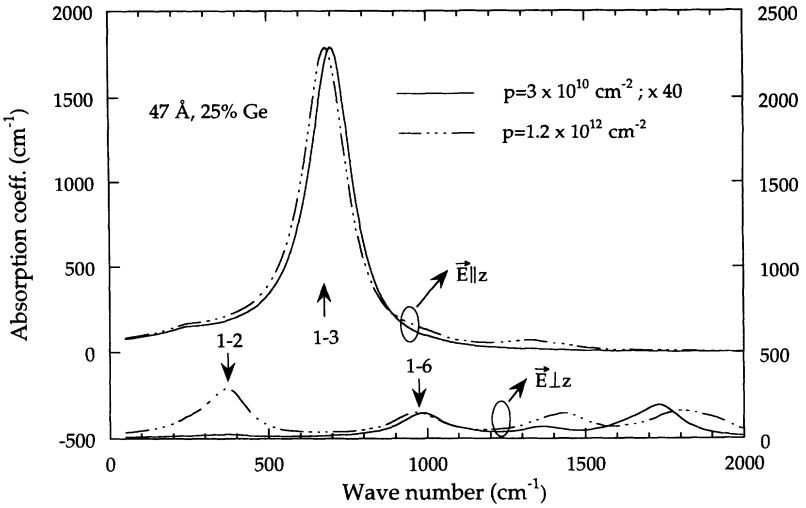

FIG. 7. Calculated absorption spectra of a ten-period p-type Si/SiGe MQW with a well width of 47 Å and a Ge content of 25% for two different doping levels [broken lines: actual doping level (1.2×10^{12} cm^{-2}), solid lines: 3×10^{10} cm^{2}]. The upper two curves (left scale) are the result for light polarized parallel to the growth direction, the lower two (right scale) for light polarized perpendicular to the growth direction. The absorption spectra of the lower doped well were multiplied by 40. The labels of the peaks in the absorption spectra indicate transitions from the ground state to energy levels counted according to Fig. 6.

state. Thus transitions from the ground state to these states are allowed for light polarized perpendicular to the growth direction even for $k_x=k_y=0$. The energies of the bands with labels greater than 6 are close to the top of the barrier and therefore the states are strongly delocalized. Furthermore the Fourier coefficients of these states are distributed among all subspaces without any significant maxima and, therefore, an interpretation of the origin of these states does not appear to be sensible.

It is well known that due to the boundary conditions for electromagnetic waves at a semiconductor-vacuum interface the electric field of light polarized *perpendicular to the interface* (p polarization) has an approximate node at the interface for total internal reflection. Thus, when the thickness of the superlattice layer is small compared to the wavelength of the incident radiation, there is a very weak coupling of the electromagnetic wave to the intersubband transitions. In contrast, if there is a metallic layer at the surface, the electric field of radiation polarized *parallel to the interface* (s polarization) has a node at the surface, whereas the electric field of the p-polarized radiation exhibits a maximum.[24] In addition, in this case the maximum absorbance of the superlattice occurs at the maximum of $\mathrm{Im}(-1/\varepsilon_{zz})$ rather than at the maximum of $\mathrm{Im}(\varepsilon_{zz})$ (Berreman effect).[21] Therefore, to include the effects of the boundary conditions, we used the dielectric tensor of the superlattice calculated as discussed above to simulate the transmission spectra of a dielectric stack consisting of substrate, superlattice, and metal layer by means of the transfer-matrix method.[35]

The results of this dielectric simulation for the sample with 47-Å wells with a Ge content of 25% are shown in Fig. 8. Covering the samples investigated in this work with a metal layer leads to a suppression of the absorption for s-polarized light and, therefore, absorption is expected only for p-polarized light. In addition, Fig. 8(a) shows that the minimum intensity of the transmitted p-polarized light is shifted by approximately 40 cm^{-1} to higher wave numbers with respect to the maximum of the absorption coefficient due to the Berreman effect.[21] For a superlattice not covered with a metal layer, due to the boundary conditions for total internal reflection on a semiconductor vacuum interface, the transmission spectrum is determined only by transitions that are allowed for light polarized perpendicular to the growth direction. Since in the geometry used in our experiments the p-polarized radiation also contains a component of the electric field perpendicular to the growth direction [see inset of Fig. 8(b)], the transmission spectra for samples without a metallic layer is calculated to be very similar in s and p polarizations, respectively [see Fig. 8(b)]. To summarize this section, a metal layer on the surface is necessary to observe p-polarized absorption in our samples, but shorts out the electric field of the s-polarized radiation. On the other hand, in waveguides without a metal on the surface, the p- and s-polarized spectra are very similar, whereas in normal-incidence experiments the interaction length is too short to yield measurable absorption in most cases. Therefore it is hard to identify any weak s-polarized absorption unambiguously.

V. EXPERIMENTAL RESULTS AND DISCUSSION

Figures 9–12 show the normalized ratio of p- to s-polarized transmission as described in Sec. II (measured spectra: thick solid curves). Each figure shows the spec-

tra of samples taken from one wafer. Within one wafer, samples with approximately the same well widths but varying Ge content were chosen. The respective parameters are indicated in the figures. The peak absorption occurs between 480 and 1830 cm^{-1}, depending on well width and Ge content.

At first we concentrate on the samples with well widths in the range between 65 and 45 Å, and Ge contents between 20% and 30% (Figs. 9 and 10). In these samples the width of the absorption peaks is as small as 20 meV (FWHM). To our knowledge, this value represents the narrowest linewidth so far observed in *p*-type Si/SiGe quantum wells. For these quantum-well dimensions, both the HH1 and HH2 subbands are strongly confined in the

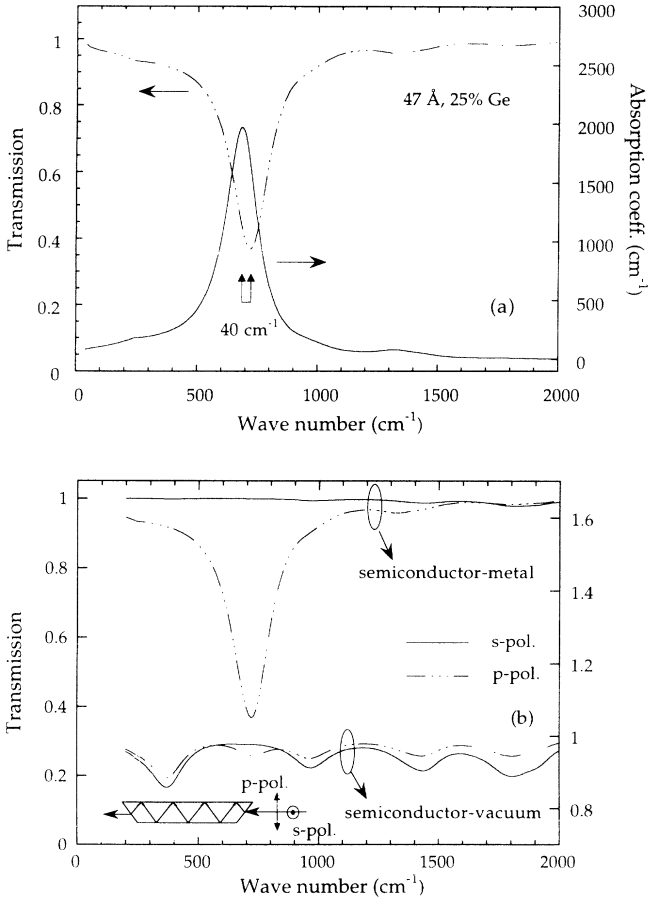

FIG. 8. (a) Simulated transmission of *p*-polarized radiation (broken line, left scale) through a MQW structure (47 Å, 25% Ge) prepared in waveguide structure and covered with a metal layer [sketched in the inset of (b)]. Also shown in (a) is the calculated absorption coefficient for light polarized parallel to the growth direction (solid line, right scale) which was used for the simulation of the waveguide transmission. Due to the Berreman effect, the minimum transmission is shifted to higher energy by approximately 40 cm^{-1} with respect to the maximum of the absorption coefficient. (b) Simulated transmission spectra for a metal-covered (upper curves, left scale) and an uncovered (lower curves, right scale) waveguide for *s* (solid lines) and *p* polarizations (broken lines). Note the crucial dependence of the transmission spectra on the waveguide preparation.

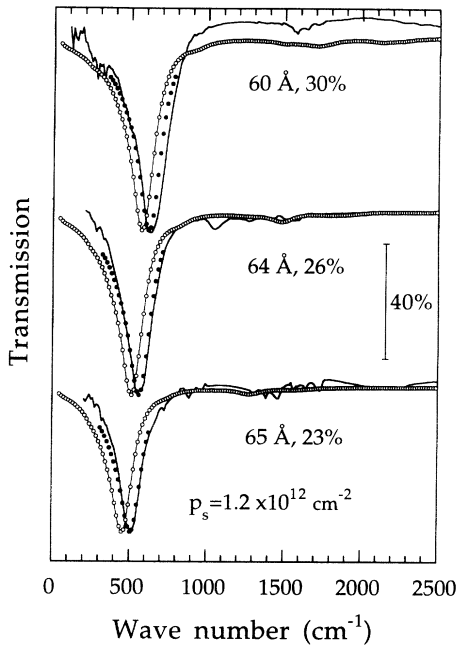

FIG. 9. Transmission spectra of three modulation-doped *p*-type Si/SiGe MQW's measured at $T=12$ K (thick, solid line). The respective Ge content and the width of the quantum wells taken from x-ray measurements are indicated in the plot. The open symbols connected by the thin lines result from calculating the absorption spectrum without taking into account the depolarization shift, and then simulating the waveguide transmission. The full symbols results if the depolarization shift is included.

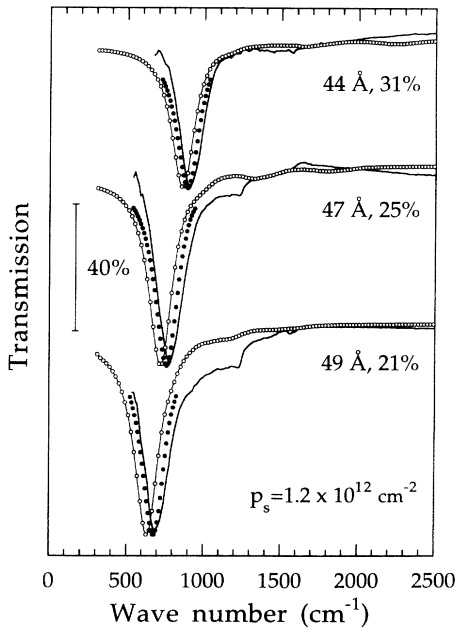

FIG. 10. Same as Fig. 9 for MQW's with narrower wells (around 45 Å).

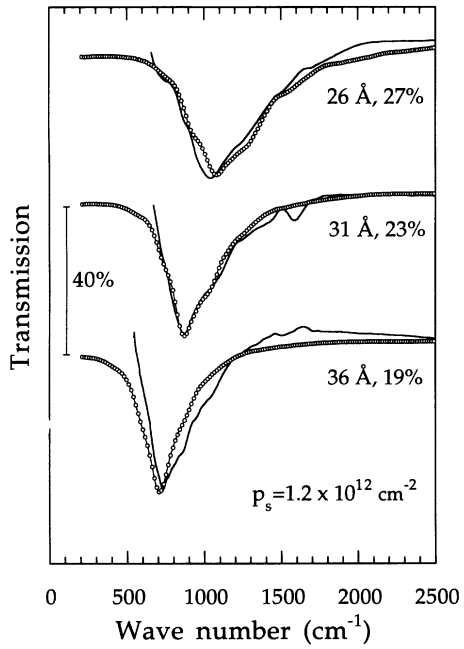

FIG. 11. Same as Fig. 9 for MQW's with narrower wells (around 30 Å). For these MQW's the shift of the absorption line due to the depolarization effect is calculated to be less than 15 cm^{-1}, which is smaller than the symbols used in this figure and, therefore, is negligible.

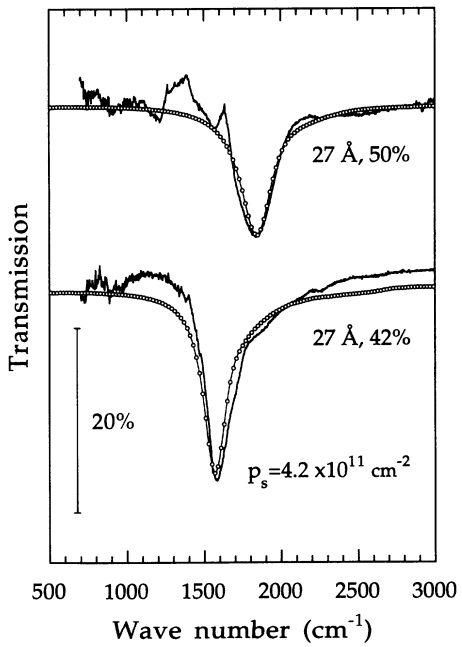

FIG. 12. Same as Fig. 9 for MQW's with a well width of 27 Å and a rather high Ge content (42 and 50%). The depolarization effect is calculated to be negligible for these samples. Due to the lower doping level of these samples, the absolute absorption is smaller.

SiGe quantum wells (compare also Fig. 5) and the absorption is due to the pure HH1-HH2 transition. The transmission spectra simulated by the procedure outlined in the preceding sections are shown by the open symbols connected by thin lines. (The absolute value of the peak absorption has been normalized to the experimental value. This required a correction factor between 0.5 and 0.8.) Obviously, there is a small but systematic deviation between measured and calculated spectra. This is due to the fact that, so far, we have not considered the depolarization shift, which is significant for the present doping levels. As mentioned above, the strongest absorption line is due to transitions predominantly within the heavy-hole subspace (HH1-HH2). Therefore, we have calculated the depolarization shift for this peak according to Ref. 36 in a one-band model for the heavy holes, which is accurate for transitions at $k_x = k_y = 0$. The full symbols in Figs. 9 and 10 indicate the shift of the strongest line in the transmission spectra due to the depolarization effect.[36] The agreement between measured and calculated transmission spectra is now indeed remarkable.

In Fig. 11 the transmission spectra for the samples with well widths between 26 and 36 Å and Ge contents between 19% and 27% are shown. In these samples the width of the absorption is much larger and also shows a fine structure on the high-energy side. This is due to fact that for such quantum-well dimensions the excited states with the highest oscillator strength are close to the top of the barrier. For illustration, the heavy-hole energy levels at $k_x = k_y = 0$ for the MQW with 31-Å wells and 23% Ge content are shown in Fig. 13 together with the relevant oscillator strengths. The HH1-HH2 transition is only weakly allowed, since the HH2 wave function is localized mainly in the barriers. The absorption is then dominated by transitions from HH1 to HH3, HH4, and HH5. All these possible final states are significantly broadened through their miniband dispersion, since they already extend into the continuum. Therefore, the absorption is a superposition of transitions to several states with finite miniband width, which is the cause of the observed linewidth and the fine structure. These features are very well reproduced by the calculated spectra, as seen in Fig. 11. The depolarization shift plays only a negligible role for samples with a quantum well thinner than 40 Å, since it is calculated to be less than 15 cm^{-1}, which is smaller than the size of the symbols used in Figs. 9–12.

Finally, we present the transmission data of two samples with a relatively high Ge content (42% and 50%) in Fig. 12. Here the excited states are again confined to the quantum wells and the absorption lines become narrow and Lorentzian (Fig. 12), because they are mainly due to the HH1-HH2 transition. The absolute absorption is somewhat smaller in these structures due to the smaller hole concentration.

We have also tried to measure the intersubband transitions that are allowed for light polarized perpendicular to the growth direction with normal incident radiation. According to our calculation, for these transitions the maximum absorption coefficient is smaller than 300 cm^{-1} (see Fig. 7). Consequently, in this geometry the expected absorbance is less than 1%, which is below the noise level of

our experiments. By using the waveguide geometry without a metal layer on MQW layers, the absorbance of the light polarized perpendicular to the growth direction is increased due to multiple reflections. However, according to Fig. 8(b), in this case the absorption spectra for p- and s-polarized light are very similar. Consequently, by calculating the ratio of the transmitted intensities of p- and s-polarized light one loses nearly all information about the absorption. On the other hand, normalizing the sample spectrum only to a reference spectrum measured with a Si substrate waveguide introduces some additional experimental error, since, due to sample preparation, two different waveguide always have slightly different transmission characteristics. We believe that these are the reasons why intersubband absorption for light polarized perpendicular to the growth direction could not be observed in this work.

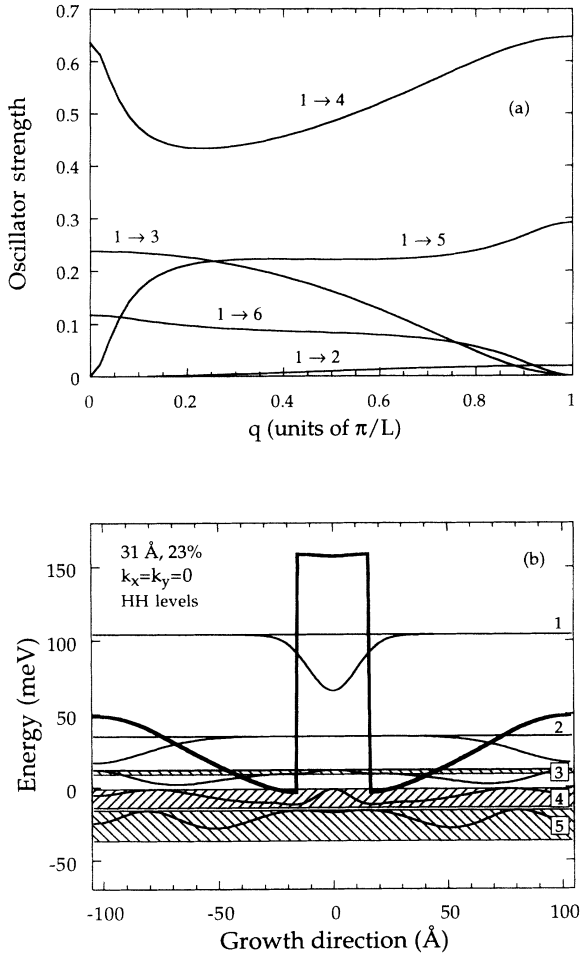

FIG. 13. Results of the self-consistent calculation of the quantum-well states in a 31-Å well with a Ge content of 23% at $k_x = k_y = 0$. As for vanishing in-plane wave vector, only HH transitions are allowed for light polarized parallel to the growth direction; only these levels are included in the plot. For this polarization, in (a), the oscillator strengths for transitions from the HH ground state to the first five excited HH states are plotted vs the reduced wave vector along the growth direction (L denotes the period in the growth direction). The self-consistent potential, the energy bands, and the squared moduli of the envelope functions corresponding to the states of the lower miniband edges are plotted in (b). The final states with the highest oscillator strength (labeled 4) already exhibit significant miniband broadening.

In several recent publications[15–18] authors reported about hole intersubband absorption in SiGe quantum wells for light polarized both parallel and perpendicular to the growth direction. In most of these publications[15,16,18] samples are investigated that have a carrier sheet concentration which is ten times higher than the sheet concentration of the samples in this work. The observed intersubband absorption is very broad (typically more than 100 meV) and shows little structure. Attempts to calculate the line shape in these experiments[15] have been impeded by the high carrier concentration, which makes many-body interactions difficult to handle. In particular, according to Ref. 15 the shape of the absorption lines is dominated by the depolarization shift, which therefore, can no longer be treated in the simple approximation of Ref. 36. Although the results of Ref. 15 were able to explain the broadening of the absorption lines, there still remained a significant difference between theory and experiment. Consequently, a quantitative correlation of the position and shape of the absorption peak with the structural parameters of the quantum wells did not appear sensible.

People *et al.*[17] reported absorption measurements on a sample doped in the SiGe quantum wells supported by band-structure calculations, but due to the lack of systematic parameter variation the origin of the observed absorption is not made totally clear.

To summarize this discussion, excellent agreement between measured and calculated transmission spectra has been achieved for a wide range of quantum-well depths and thicknesses. We point out that a *consistent* interpretation of *all* data is only possible at the present level of sophistication, i.e., self-consistent calculation of the energy levels including many-body effects, the depolarization shift, and the Berreman effect. The only fitting parameters were a constant correction factor for the absolute absorption value, which is slightly different for each sample (this might be due to small uncertainties in the exact hole concentrations) and one phenomenological broadening parameter. The peak position and the line shape are not adjustable in our calculation, but follow directly from the calculated band structure.

VI. CONCLUSIONS

We have performed an extensive theoretical and experimental study of intersubband transitions in modulation-doped p-type SiGe multiple quantum wells with various Ge contents and well widths. Because of the mixing of heavy-hole, light-hole, and spin-split-off valence bands due to the confining potential and the strain, intersubband absorption is allowed, in principle, for light polarized both perpendicular and parallel to the growth direction. However, our calculations show that for the present doping levels the dominant contribution to the absorption originates from transitions between heavy-hole states, which are allowed only for light polarized

parallel to the growth direction. Moreover, the contributions polarized perpendicular to the growth direction are even suppressed in our experimental geometry, which is essentially a waveguide with a metal layer on top.

To our knowledge, the intersubband absorption observed in this work exhibits the narrowest linewidth so far observed in SiGe *p*-type quantum wells. Using the structural parameters determined by high-resolution triple-axis x-ray diffraction, we obtain excellent agreement between measurement and theory. However, it is necessary to include the in-plane dispersion of the quantum-well states as well as many-body effects like the Hartree potential, exchange-correlation interaction, and depolarization shift in the calculation.

ACKNOWLEDGMENTS

This work is supported in part by ESPRIT Basic Research Action 7128, and by the FWF under Project No. 9119.

[1] *Intersubband Transitions in Quantum Wells,* edited by E. Rosencher, B. Vinter, and B. Levine (Plenum, New York, 1992).

[2] J. Faist, F. Capasso, D. L. Sivco, C. Sirtori, A. L. Hutchinson, and A. Y. Cho, Science **264**, 553 (1994).

[3] B. F. Levine, J. Appl. Phys. **74**, R1 (1993).

[4] *Semiconductor Quantum Wells and Superlattices for Long-Wavelength Infrared Detectors,* edited by M. O. Manasreh (Artech House, Boston, 1993).

[5] E. A. Fitzgerald, Y. H. Xie, M. L. Green, D. Brasen, A. R. Kortan, J. Michel, Y. J. Mii, and B. E. Weir, Appl. Phys. Lett. **59**, 811 (1991).

[6] F. K. LeGoues, B. S. Meyerson, and J. F. Morar, Phys. Rev. Lett. **66**, 2903 (1991).

[7] F. Schäffler, D. Többen, H. J. Herzog, G. Abstreiter, and B. Holländer, Semicond. Sci. Technol. **7**, 260 (1992).

[8] M. M. Rieger and P. Vogl, Phys. Rev. B **48**, 14 276 (1993).

[9] H. Hertle, G. Schuberth, E. Gornik, G. Abstreiter, and F. Schäffler, Appl. Phys. Lett. **59**, 2977 (1991); H. Hertle, F. Schäffler, A. Zrenner, G. Abstreiter, and E. Gornik, Thin Solid Films **222**, 20 (1992).

[10] K. Fujita, S. Fukatsu, Y. Shiraki, H. Yaguchi, and R. Ito, Appl. Phys. Lett. **61**, 210 (1992).

[11] C. Lee and K. L. Wang, Appl. Phys. Lett. **60**, 2264 (1992).

[12] C. Lee and K. L. Wang, Appl. Phys. Lett. **64**, 1256 (1994).

[13] E. R. Brown and S. J. Eglash, Phys. Rev. B **41**, 7559 (1990).

[14] Y. C. Chang and R. B. James, Phys. Rev. B **39**, 12 672 (1989).

[15] S. K. Chun, D. S. Pan, and K. L. Wang, Phys. Rev. B **47**, 15 638 (1993).

[16] R. P. G. Karunasiri, J. S. Park, and K. L. Wang, Appl. Phys. Lett. **61**, 2434 (1992).

[17] P. People, J. C. Bean, C. G. Bethea, S. K. Sputz, and L. J. Peticolas, Appl. Phys. Lett. **61**, 1122 (1992).

[18] R. P. G. Karunasiri, J. S. Park, Y. J. Mii, and K. L. Wang, Appl. Phys. Lett. **57**, 2585 (1990); J. S. Park, R. P. G. Karunasiri, Y. J. Mii, and K. L. Wang, *ibid.* **58**, 1083 (1990); R. P. G. Karunasiri, J. S. Park, and K. L. Wang, *ibid.* **59**, 2588 (1991).

[19] M. J. Shaw, K. B. Wong, E. Corbin, and M. Jaros, Solid State Electron. **37**, 1303 (1994).

[20] J. M. Luttinger and W. Kohn, Phys. Rev. **97**, 869 (1955).

[21] B. Harbecke, B. Heinz, and P. Grosse, Appl. Phys. A **38**, 263 (1985), and references therein.

[22] W. J. Bartels, Acta Crystallogr. A **42**, 539 (1986).

[23] E. Koppensteiner, P. Hamberger, G. Bauer, A. Pesek, H. Kibbel, H. Presting, and E. Kasper, Appl. Phys. Lett. **62**, 1783 (1993).

[24] M. J. Kane, M. T. Emeny, N. Apsley, C. R. Whitehouse, and D. Lee, Semicond. Sci. Technol. **3**, 722 (1988).

[25] G. L. Bir and G. E. Pikus, *Symmetry and Strain-Induced Effects in Semiconductors* (Wiley, New York, 1974).

[26] R. People and S. K. Sputz, Phys. Rev. B **41**, 8431 (1990).

[27] F. H. Pollak and M. Cardona, Phys. Rev. **172**, 816 (1968).

[28] D. Bimberg, R. Blachnik, M. Cardona, P. J. Dean, Th. Grave, G. Harbeke, K. Hübner, U. Kaufmann, W. Kress, O. Madelung, W. von Münch, U. Rössler, J. Schneider, M. Schultz, and M. S. Skolnick, in *Numerical Data and Functional Relationships in Science and Technology,* edited by O. Madelung, Landolt-Börnstein, New Series, Group III, Vol. 17, Pt. a (Springer-Verlag, Berlin, 1982).

[29] M. G. Burt, Semicond. Sci. Technol. **3**, 739 (1988); M. G. Burt, J. Phys. Condens. Matter **4**, 6651 (1992).

[30] G. A. Baraff and D. Gershoni, Phys. Rev. B **43**, 4011 (1991).

[31] L. Colombo, R. Resta, and S. Baroni, Phys. Rev. B **44**, 5572 (1991).

[32] C. G. Van de Walle and R. M. Martin, Phys. Rev. B **34**, 5621 (1986).

[33] W. L. Bloss, J. Appl. Phys. **66**, 3639 (1989).

[34] L. Hedin and B. I. Lundqvist, J. Phys. C **4**, 2064 (1971).

[35] See, for example, B. Harbecke, Appl. Phys. B **39**, 165 (1986).

[36] S. J. Allen, Jr., D. C. Tsui, and B. Vinter, Solid State Commun. **20**, 425 (1976); T. Ando, *ibid.* **21**, 133 (1977).